A phase-field model investigating the role of elastic strain energy during the growth of closely spaced neighbouring interphase precipitates

Alireza Rahnama[1*], Samuel Clark[1,2], Vit Janik[1,3], Seetharaman Sridhar[1,4]

1 Advanced Steel Research Centre, University of Warwick, CV4 7AL, United Kingdom
2 School of Materials, University of Manchester, Manchester, M13 9PL, United Kingdom
3 Faculty Research Centre for Manufacturing and Materials Engineering, Coventry University, Coventry, CV1 5FB, United Kingdom
4 George S. Ansell Department of Metallurgical and Materials Engineering, Colorado School of Mines, Golden, CO 80401, USA

Abstract

A multi-phase field method is developed to investigate the effects of transformation strain on the transformation kinetics, thermodynamic stability and pairing of interphase precipitates in micro-alloyed steels. The model conserves homogeneity of stress in the diffuse interface between elastically inhomogeneous phases and provides an explanation of the mechanism resulting in the pairing of two adjacent interphase precipitates. Several scenarios of inhomogeneous elastic conditions have been considered. The simulations for a situation where only the interfacial energy is considered to contribute to the transformation show that this energy can lead to the establishment of a neck between two neighbouring precipitates. However, if sufficient time is given, one of the precipitates will completely dissolve into its neighbouring particle. On the other hand, when both strain and interfacial energies act on the system, the bridge between the particles becomes stabilised leading to the pairing of the particles. This is a result of the particles tendency to minimise the strain energy due to the excessive strain field generated by the neck between the two particles.

*Corresponding author
Email addresses: A.Rahnama@warwick.ac.uk (Alireza Rahnama[1]), S.J.Clark@warwick.ac.uk (Samuel Clark[1,2]), V.Janik@warwick.ac.uk (Vit Janik[1,3]), S.Seetharaman@warwick.ac.uk (Seetharaman Sridhar[1,4])

Keywords: Micro-alloyed steel, Phase-field, Elastic strain energy, Precipitate pairing
2010 MSC: 00-01, 99-00

1. Introduction

Interphase precipitation in steels is characterised by periodic parallel planes of randomly orientated carbide precipitates which form at the interphase between the austenite and ferrite as the former decomposes into the later [1]. Interphase precipitation is often found in ferritic steels when the steel is alloyed with one or several strong carbide forming elements such as V, Nb or Ti [2]. It has been found that a single-phase ferritic matrix in low carbon steels strengthened by periodic arrangement of interphase carbide precipitates offers a high strength, high formability, and low-cost structural material, suitable for large scale production of automotive sheet [3, 4].

Interphase precipitates are found in allotriomorphic α ferrite which itself is considered to grow on either side of a prior γ austenite grain boundary, with at least one interphase boundary adopting a low energy, semi-coherent, orientation relationship [5], such as the Kurdjumov-Sachs (KS) [6], or the Nishiyama-Wasserman (NW) [7, 8] orientation relationships (OR). A growth ledge on a semi-coherent γ/α interphase boundary consists of a disordered, mobile riser and a comparatively coherent and immobile tread [9]. Typically, it is thought that the nucleation of interphase precipitates occurs on ledged γ/α interphase boundaries [1]. Although the high-energy interphase boundary of the riser would be favourable for the nucleation of precipitates through the formation of abutted spherical cap nuclei [10], and further eased by the segregation of substitutional solutes through the solute drag effect [11], interphase precipitates are however observed to have nucleated on the comparatively low energy γ/α tread [12]. This is thought to be because there would be an insufficient time for successful stable nuclei to form on the mobile riser. Further, implications of nucleation on the low energy tread are as follows:

- As the interfacial energy of the ledged interphase boundary tread is low, therefore a precipitate nuclei would subsequently be expected to be nearly spherical [10].

- The nucleation of interphase precipitates is not aided by the segregation of substitutional alloying elements as they are not thought to be able to readily segregate to the mobile, low energy tread of the semi-coherent γ/α interphase boundary [11].

In a single study, it has been observed using TEM that in some circumstances disc shaped interphase precipitates can join at the tips and form pairs of connected precipitates [13]. The reason for the paucity of TEM observations of connected precipitates is that unless the planes of interphase carbides are suitably spread it is impossible to tilt a specimen such that an individual plane can be imaged [14]. Re-examination of the images by Davenport and Honeycombe [14] does, however, confirm that individual carbide precipitates located on planar rows of interphase precipitates often interact with one another. It is hypothesized that the phenomenon of precipitate-precipitate interactions on the densely populated planes of interphase precipitates, may, in fact, be commonplace.

In our previous paper [15], a multi-component phase field method (PFM) model was derived which was coupled with a multi-component CALPHAD thermodynamic database using a four-sublattice model. Such models, including the phase-field method or other time-dependant Ginzburg-Landau methods, are a powerful means of encapsulating the complex interactions between atomistic mechanisms and macroscopic conditions on the mesoscopic scale [16]. In the phase-field method, the continuum field variables can be identified with the phase field (structural order parameter) ϕ_α with temperature *T*, concentration $\overrightarrow{c}$, total strain ϵ^{ij}, magnetisation m^i or other variables relevant to describe the system of interest.

The premise of this work is to extend our model [15] by investigating the effect of the previously neglected elastic transformation strain upon the transformation kinetics, thermodynamic stability, and pairing and necking of interphase precipitates in microalloyed steels. The elastic transformation strain associated with precipitation is known to have a potent influence upon the morphology of said precipitates. A coherent hard

precipitate (nuclei) in an isotropic matrix would be expected to adopt the morphology of a sphere [17] to minimize the elastic strain energy whereas a soft coherent precipitate would result in an oblate spheroid. In contrast, Nabarro [18], mathematically explored the role of strain upon the morphology of incoherent precipitates within an isotropic matrix. The elastic strain associated with interphase precipitates is hypothesized to play an important role in the growth of individual precipitates and the interactions between neighbouring precipitates, explaining the complex, compound morphologies, and particularly the necking behaviour of interphase carbide precipitates.

2. Model

The model considers the growth and interaction between precipitates in-terms of transformation strain upon low energy γ/α ledged interphase boundary treads. In 3D space, for the problem with total strain ϵ^{ij} in the two directions *i*, *j* in terms of the phase strain ϵ_α^{ij} in each individual phase (α), we have:

$$\epsilon^{ij} = \sum_\alpha \phi_\alpha h_\alpha(\epsilon_\alpha^{ij}) \tag{1}$$

h_α is dependant on the elastic properties of each individual phase and ϕ_α is the field variable for phase α. Eq.1 calculates the total strain as a linear summation of the strains of the individual phases α weighted by the phase densities ϕ_α. In other words, this equation is a direct extension of original multi phase function for diffusive phase transformations [16]. To correlate the strain fields in the different phases equal elastic stresses in the interface are assumed.

2.1. The mechanical multi-phase model

The free energy can be defined as an integral of the density functional over the domain Ω. The density functional consists of the grain boundary energy density f^{gb},

the chemical free energy density f^{ch}, and the elastic energy density f^{el}. we have:

$$F = \int_{\Omega} f^{gb} + f^{ch} + f^{el} \tag{2}$$

where,

$$f^{gb} = \sum_{\alpha,\beta=1}^{N} \frac{4\alpha_{\alpha\beta}}{\gamma_{\alpha\beta}} \{ \frac{\gamma_{\alpha\beta}^2}{\pi^2} |\nabla\phi_\alpha . \nabla\phi_\beta| + w_{\alpha\beta} \} \tag{3}$$

where, $\alpha_{\alpha\beta}$ refers to the grain boundary energy between different phases. Subscript α and β refers to the relevant pair from ferrite, austenite or precipitate. $\gamma_{\alpha\beta}$ refers to the interface width and $w_{\alpha\beta}$ is the dimensionless repulsive potential function that keeps the interface upright [19]. $w_{\alpha\beta} = \phi_\alpha \phi_\beta$ when $0 < \phi_{\alpha/\beta} < 1$ and ∞ elsewhere. This specific form of Eq. 3 follows the scaling invariance of the total interface energy as an integral over f^{gb} with respect to the interface width $\gamma_{\alpha\beta}$.

f^{ch} is expressed as:

$$f^{ch} = \sum_{\alpha=1}^{N} \phi_\alpha f_\alpha(\overrightarrow{c}_\alpha) + \overrightarrow{\mu}(\overrightarrow{c} - \sum_{\alpha=1}^{N} \phi_\alpha \overrightarrow{c}_\alpha) \tag{4}$$

$f_\alpha(\overrightarrow{c}_\alpha)$ is the bulk free energy of each individual phase, which depends on the phase concentrations $\overrightarrow{c}_\alpha$. $\overrightarrow{\mu}$ refers to the chemical potential vector. This vector is defined as a Lagrange multiplier to account for the mass balance between the neighbouring phases. This was achieved by defining the mixture concentration $\overrightarrow{c}$, which is continuous over the interface as $\overrightarrow{c} = \sum_\alpha \phi_\alpha \overrightarrow{c}_\alpha$.

Similarly, f^{el} is defined as:

$$f^{el} = \frac{1}{2} \{ \sum_{\alpha=1}^{N} \phi_\alpha (\epsilon_\alpha^{ij} - \epsilon_\alpha^{*ij}) C_\alpha^{ijkl} (\epsilon_\alpha^{kl} - \epsilon_\alpha^{*kl}) \} \tag{5}$$

where ϵ_α^{ij} is the total strain in individual phases, ϵ_α^{*ij} is the eigenstrain and C_α^{ijkl} is the Hook's matrix (Young's modulus). It is noted that ϵ_α^{*ij} and C_α^{ijkl} are concentration and temperature-dependant, however in the present work, it is assumed that these

quantities are constant with both concentration and temperature but vary from phase to phase. To correlate the strain fields in the different phases, it is required to define an additional condition. Since $\overrightarrow{\mu} = \frac{\partial f^{ch}}{\partial \overrightarrow{c}}$, from analogy we can define the elastic stresses as $\sigma_{\alpha}^{ij} = \frac{1}{\phi_{\alpha}} \frac{\partial f^{el}}{\partial \epsilon_{\alpha}^{ij}}$. To define the additional condition, mechanical equilibrium is assumed between phases in the strong form, i.e. to solve the equations of elasticity it is required to define a domain for finding an equilibrium configuration of a deformable elastic body which is in the present case the precipitates' body. It is also assumed that a continuity of all stress components σ^{ij} exists in the interface. Thus, in the mathematical form for all α and β we have:

$$\sigma_{\alpha}^{ij} = \sigma_{\beta}^{ij} = \sigma^{ij} \tag{6}$$

Thus we have:

$$(\epsilon_{\alpha}^{ij} - \epsilon_{\alpha}^{*ij}) C_{\alpha}^{ijkl} = (\epsilon_{\beta}^{ij} - \epsilon_{\beta}^{*ij}) C_{\beta}^{ijkl} = (\epsilon^{ij} - \epsilon^{*ij}) C^{ijkl} \tag{7}$$

and

$$\epsilon^{ij} - \epsilon^{*ij} = \sigma^{kl} [C^{ijkl}]^{-1} \tag{8}$$

$\epsilon^{ij} - \epsilon^{*ij}$, ϵ^{*ij} and C^{ijkl} are the effective strain, the effective eigenstrain and the effective elasticity matrix, respectively. Effective strain and effective compliance matrix $[C^{ijkl}]^{-1}$ can be defined by a linear mixture model:

$$\epsilon^{ij} - \epsilon^{*ij} = \sum_{\alpha=1}^{N} \phi_{\alpha} (\epsilon^{ij} - \epsilon^{*ij}) \tag{9}$$

and

$$[C^{ijkl}]^{-1} = \sum_{\alpha=1}^{N} \phi_{\alpha} [C^{ijkl}]_{\alpha}^{-1} \tag{10}$$

Thus, we can express the effective elasticity matrix as:

$$C^{ijkl} = \left[\sum_{\alpha=1}^{N} \phi_\alpha [C_\alpha^{ijkl}]^{-1} \right]^{-1} \tag{11}$$

This expression of effective elasticity matrix is known as the Reuss limit for the elastic behaviour of a compound [20, 21]. The elastic energy (Eq.5) can be expressed in a reduced form as:

$$f^{el} = \frac{1}{2}(\epsilon^{ij} - \epsilon^{*ij}) C^{ijkl} (\epsilon^{kl} - \epsilon^{*kl}) \tag{12}$$

The quantities ϵ^{*ij} and C^{ijkl} vary continuously from phase to phase according to the respective properties of the phases. We may note that Eq.12 is not a linear function of ϕ_α because of the additional constraint of mechanical equilibrium applied to Eq. 5.

2.2. Kinetic equations

Kinetic equations can be defined according to the field variables $\phi_\alpha(x, y, z, t)$, $\overrightarrow{c}(x, y, z, t)$ and $\epsilon^{ij}(x, y, z, t)$:

$$\dot{\phi}_\alpha = -\sum_{\beta=1}^{N} \frac{\mu_{\alpha\beta}}{N} \left(\frac{\delta F}{\delta \phi_\alpha} - \frac{\delta F}{\delta \phi_\beta} \right) \tag{13}$$

$$\dot{\overrightarrow{c}} = \nabla \left(\sum_{\alpha=1}^{N} \overrightarrow{\overrightarrow{M}} \nabla \frac{\delta F}{\delta \overrightarrow{c}} \right) \tag{14}$$

$$0^i = \nabla^j \sigma^{ij} = \nabla^j \frac{\delta F}{\delta \epsilon^{ij}} \tag{15}$$

$\mu_{\alpha\beta}$ and $\overrightarrow{\overrightarrow{M}}$ are the interface mobility and the chemical mobility matrix, respectively. Here, we consider a double obstacle potential [16], the multi phase field equation can be expressed as:

$$\dot{\phi}_\alpha = \sum_{\beta=1}^{N} \frac{\mu_{\alpha\beta}}{N} \left\{ \sum_{\gamma=1}^{N} [\sigma_{\beta\gamma} I_{\beta\gamma} - \sigma_{\alpha\gamma} I_{\alpha\gamma}] + \Delta G_{\alpha\beta} \right\} \tag{16}$$

where,

$$I_{\alpha\gamma} = \frac{8}{\gamma_{\alpha\gamma}}\left[\delta_\alpha \frac{\gamma_{\alpha\gamma}^2}{\pi^2}\nabla^2\phi_\gamma + \delta_\alpha\phi_\gamma\right] \tag{17}$$

$I_{\alpha\gamma}$ denotes the generalised curvature terms and $\delta = 0$ if $\phi_\alpha = 0$ and $\delta = 1$ elsewhere. In Eq.16, $\Delta G_{\alpha\beta}$ is the local deviation from thermodynamic equilibrium and consists of the chemical and the elastic components because only these two components are assumed to be at equilibrium at the interface:

$$\Delta G_{\alpha\beta} = \Delta G_{\alpha\beta}^{ch} + \Delta G_{\alpha\beta}^{el} \tag{18}$$

For the chemical non-equilibrium contribution $\Delta G_{\alpha\beta}^{ch}$, we have:

$$\Delta G_{\alpha\beta}^{ch} = -\left(\frac{\partial}{\partial\phi_\alpha} - \frac{\partial}{\partial\phi_\beta}\right) f^{ch} = -f_\alpha(\overrightarrow{c}_\alpha) + f_\beta(\overrightarrow{c}_\beta) + \overrightarrow{\mu}(\overrightarrow{c}_\alpha - \overrightarrow{c}_\beta) \tag{19}$$

Similarly, $\Delta G_{\alpha\beta}^{el}$ can be expressed as follows:

$$\Delta G_{\alpha\beta}^{el} = -\left(\frac{\partial}{\partial\phi_\alpha} - \frac{\partial}{\partial\phi_\beta}\right) f^{el} = (\epsilon^{ij} - \epsilon^{*ij})C^{ijkl} \left\{(\epsilon_\alpha^{*ij} - \epsilon_\beta^{*ij}) - \frac{1}{2}\Big([C_\alpha^{ijkl}]^{-1} - [C_\beta^{ijkl}]^{-1}\Big)C^{mnop}(\epsilon^{op} - \epsilon^{*op})\right\} \tag{20}$$

$(\epsilon_\alpha^{*ij} - \epsilon_\beta^{*ij})$ in Eq.20 takes into account the difference in eigenstrain between the phases involved in transformation. $([C_\alpha^{ijkl}]^{-1} - [C_\beta^{ijkl}]^{-1})$ determines the difference in elasticity. $(\epsilon^{ij} - \epsilon^{*ij})C^{ijkl}$ is the linear-dependency on the local elastic stress state, i.e. based on the sign of the local stress this term determines if a phase transformation with expansion or contraction will be favoured or hindered. Eq.14 can be rewritten in terms of diffusion matrices as:

$$\dot{\overrightarrow{c}} = \nabla\left(\sum_{\alpha=1}^{N}\phi_\alpha \overrightarrow{\overrightarrow{M}}_\alpha \nabla\frac{\partial f_\alpha}{\partial\overrightarrow{c}_\alpha}\right) = \nabla\left(\sum_{\alpha=1}^{N}\phi_\alpha \overrightarrow{\overrightarrow{D}}_\alpha \nabla\overrightarrow{c}_\alpha\right) \tag{21}$$

where $\overrightarrow{\overrightarrow{M}}$ is chemical mobility matrices defined as $\overrightarrow{\overrightarrow{M}} = \sum_{\alpha=1}^{N} \phi \overrightarrow{\overrightarrow{M}}_{\alpha}$. $\overrightarrow{\overrightarrow{D}}$ is diffusion matrices defined as $\overrightarrow{\overrightarrow{D}} = \overrightarrow{\overrightarrow{M}}_{\alpha}\left(\frac{\partial^2 f_{\alpha}}{\partial \overrightarrow{c}_{\alpha} \partial \overrightarrow{c}_{\beta}}\right)$. From the parallel tangent rule $\frac{\partial f_{\alpha}}{\partial \overrightarrow{c}_{\alpha}} = \frac{\partial f_{\beta}}{\partial \overrightarrow{c}_{\beta}} = \overrightarrow{\mu}$, the quasi equilibrium concentrations $\overrightarrow{c}^{0}_{\alpha\beta}$ (function in space and time) can be determined for a pair of phases α and β and for a given mixture concentration $\overrightarrow{c}$. Thus, the phase concentrations can be formulated according to these concentrations [22, 23]:

$$\Delta \overrightarrow{c}_{\alpha} = \overrightarrow{c}_{\alpha} - \overrightarrow{c}^{0}_{\alpha\beta} \tag{22}$$

Substituting the relationship obtained from tangent rule into Eq.22, we have:

$$\Delta \overrightarrow{c}_{\alpha} = \Delta \overrightarrow{c}_{\beta} \frac{\partial \overrightarrow{c}_{\alpha}}{\partial \overrightarrow{c}_{\beta}} = \Delta \overrightarrow{c}_{\beta} \frac{\partial f_c^{\beta}}{\partial f_c^{\alpha}} \frac{\partial \overrightarrow{c}_{\alpha}}{\partial \overrightarrow{c}_{\beta}} = \Delta \overrightarrow{c}_{\beta} \frac{f_{cc}^{\beta}}{f_{cc}^{\alpha}} = \Delta \overrightarrow{c}_{\beta} \overrightarrow{\overrightarrow{k}}_{\alpha\beta} \tag{23}$$

Here we introduced the abbreviation $f_c^{\alpha} = \frac{\partial f_{\alpha}}{\partial \overrightarrow{c}_{\alpha}}$ and a generalized partitioning coefficient is $\overrightarrow{\overrightarrow{k}}_{\alpha\beta}$ used. Using $\overrightarrow{c} = \sum_{\alpha} \phi_{\alpha} \overrightarrow{c}_{\alpha}$, Eq.22 and Eq.23 the phase concentrations can be eliminated and Eq.14 can be rewritten as:

$$\dot{\overrightarrow{c}} = \nabla \left(\sum_{\alpha=1}^{N} \phi_{\alpha} \overrightarrow{\overrightarrow{D}}_{\alpha} \nabla \frac{\left(\overrightarrow{c} - \sum_{\beta=1}^{N} \phi_{\beta} \left(\overrightarrow{c}^{0}_{\beta\alpha} \overrightarrow{\overrightarrow{k}}_{\beta\alpha} \overrightarrow{c}^{0}_{\alpha\beta} \right) \right)}{\sum_{\beta=1}^{N} \phi_{\beta} \overrightarrow{\overrightarrow{k}}_{\beta\alpha}} \right) \tag{24}$$

The derivation for $\dot{\overrightarrow{c}}$ in Eq.24 is similar to the one expressed in Ref.[24] with a different expression for the diffusion matrix. This is done to eliminate the unknown $\overrightarrow{c}_{\alpha}$ using the local linearisation, thereby enabling efficient numerical solution.

2.3. Solution procedure, case study and experimental validation

The composition of the micro-alloyed steel considered in this work is, Fe-1.962C-0.748Mn-0.312V (all in at.%) [25, 26]. The generalized chemical potential $\overrightarrow{\mu}$ in the chemical non-equilibrium contribution (Eq.19) is computed iteratively for a given average concentration $\overrightarrow{c}$ and a given set of phase field ϕ_{α} by the minimization of the

total free energy described by the free energy functions $f_\alpha(\overrightarrow{c}_\alpha)$.

The displacements are calculated using the principle of relaxation to mechanical equilibrium (Eq.15), i.e. this equation is numerically solved for the displacement vector u^i using $\epsilon^{ij} = \frac{1}{2}(\frac{\partial}{\partial u^i}u^i + \frac{\partial}{\partial u^j}u^j)$ in the weak formulation by linear finite elements. C_{11} and C_{12} are considered to be 280 GPa and 120 GPa, respectively. The dimensionless elastic constants for the individual phases α (matrix) were defined as $C^\alpha_{11} = \frac{(1-\nu)}{1-2\nu} \times C^\alpha_{44}$ and $C^\alpha_{12} = \frac{\nu}{1-2\nu} \times C^\alpha_{44}$. The eigenstrain ϵ^* is 1% and σ_0 1980 MPa. We define a parameter $h = \frac{C^\beta_{44}}{C^\alpha_{44}}$ in order to compare the strength of the precipitates with that of matrix. In addition, we define a scaled strain parameter $\overline{\eta} = \eta\sqrt{\frac{E}{\rho_0 k_B T(1-\nu)}}\left(\frac{2}{c^\beta - c^\alpha}\right)^2$ where η is the strain parameter that strongly depends on the composition of the material. Here we adopted $\eta = 0.126$ [27]. η determines the dilatational strain due to the compositional change according to Vegard's law, $\eta = \frac{\mathbf{e}}{c-c_0}$ [28] where c_0 is the stress-free composition. ρ_0 is density, k_B Boltzman constant, T temperature, and ν Possion ratio. All displacements are placed at the corners of a square grid and the physical properties are assumed to be constant over the control volume. The stiffness tensor of any intermediate phase (IP) formed during the particles interactions was assumed to take an intermediate value, e.g. $C^{IP} = \frac{C^\aleph + C^\beta}{2}$. The boundary conditions used for the current calculations are free volume expansions/contractions while keeping the rectangular shape of the calculation grid.

The chemical Gibbs energies, mobilities and diffusion coefficients are taken from Ref. [15]. The interfacial energy is taken as isotropic, $\sigma = 5 \times 10^{-5}$ J/cm^2 for the interface between ferrite and austenite [29]. The interface between precipitates and austenite γ and ferrite α are assumed to be semi-coherent with similar interfacial energies of $\sigma = 2 \times 10^{-5}$ J/cm^2 and $\sigma = 2.5 \times 10^{-5}$ J/cm^2, respectively. The interfacial energies are selected within the range of interfacial energies proposed by Howe [30] for semi-coherent interphase boundaries. Due to the similar values of the precipitate/matrix interfacial energies, the modelled results of the interphase boundary precipitates, considered in this work would be similar to the case where precipitates were placed fully within either matrix phase. At the nucleation stage, two particles are

placed at the γ/α interphase boundary assuming a of radius 1 nm. We define:

- *Necking* - as a metastable stage where ϕ in the bridge between the neighbouring precipitates have an intermediate value.
- *Pairing* - as a stage of the transformation encountered where ϕ in the bridge between the neighbouring precipitates has a value equal to that of precipitates.

The domain size was $300\times300\times300$ cells with a discretization of $\Delta x = 0.25$ nm. The interface width is considered to be $\gamma = 6$ cells. The time discretization is set as 10^{-2}. Instantaneous relation to mechanical equilibrium is considered for every time step.

Multi-Component PFM microstructural simulations produce a spatially and time resolved distribution of alloying elements. This lends the results of such simulations to be validated against elemental distribution mapping techniques such as STEM-EDS which offer a sufficient resolution on nano-scale. For the purposes of qualitative validation of the model, Figure 1 is presented showing STEM-EDS map (V-Kα) of VC interphase precipitates, representative of a broader microstructure of an industrial HSLA steel obtained after typical thermo-mechanical processing finished with controlled coiling at $630°$C. The alloy in question has a similar V composition to that of the modelled alloy providing a suitable means of qualitatively validating the PFM model in this work. In Figure 1 specific cases highlighting specific conditions of interphase precipitates have been identified: 1) a neck has faintly formed joining two spaced precipitates (black box), 2) a neck has formed between two precipitates (magenta box), and 3) a case where several precipitates have paired together (orange box). A FEG-TEM FEI microscope model Talos F200X, operating at 200 kV with four integrated Super-X SDD EDS detectors at a detection angle of 0.9 rad was used for elemental mapping of vanadium. Samples were prepared from industrial coil using a focused ion beam (FIB) lift-out method, foils were thinned down to approximately 120 nm in thickness, using a final gentle low voltage cleaning step.

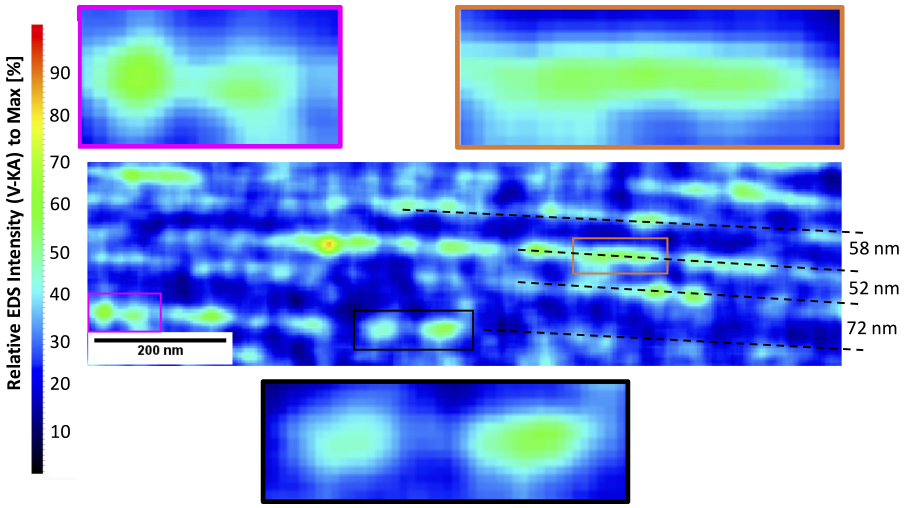

Figure 1: STEM-EDS mapping (V-Kα) of an industrial HSLA steel showing rows of interphase precipitates; expanded sections illustrate selected cases exhibiting specific conditions of interphase precipitates: a neck begins to form (black box), a neck between two precipitates has become established (magenta box), and a case where several precipitates have paired together (orange box).

3. Results and discussion

Fig.2 shows the interaction between two neighbouring precipitates with almost equal radii ($\overline{r}$) which is a dimensionless quantity. We consider two growth mechanisms for the precipitates presented in Fig.2: interfacial energy assumed to be the only contributing energy (Fig.2a1-a3), and both strain and interfacial energy considered to contribute to the growth of the precipitates. The spacing between the adjacent precipitates is assumed to be $\overline{d} = \frac{\overline{r}}{3}$ ($\overline{d}$ is a dimensionless quantity).. Throughout the course of the interaction, the precipitates develop necking without any contribution from the strain energy because $\overline{\eta} = 0$. The diffusion distance between the particles was small so that surface tensions rapidly activated precipitation that bridged the two particles. The pronounced curvature gradients then occurred because of the established bridge between the two particles. The curvature gradients then, in turn, lead to the formation of a single precipitate with uniform curvature at the interface. In the second scenario Fig.2b1-b3, forced necking occurred and the strain energy and the resultant stresses drive atoms to the region with minimal distance between the adjacent particles. The two precipitates thus coalesced and paired with each other.

As is evident from these simulations, both interfacial and elastic energy result in the establishment of a bridge between the adjacent particles, however, it is the strain energy that leads to a stable pairing of the particles, provided that enough time is given to the precipitates to grow. With sufficient elapsed time the interfacial energy causes the dissolution of the particle into its adjacent neighbour, while in the second scenario, strain energy became the dominating contributory energy that leads to the decrease of the excessive tension between the two particles.

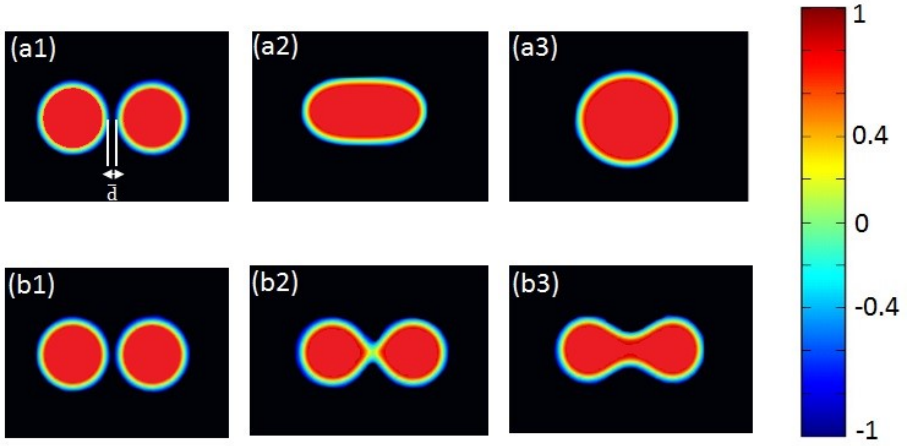

Figure 2: Interaction of two neighbouring precipitates; $\overline{d}$ is the initial distance between the precipitates ($\overline{d} = \frac{\overline{r}}{3}$). Note that $\overline{r}$ (the initial radii) of precipitates is dimensionless. (a) Necking mechanism of neighbouring precipitates without strain effects. (b) Necking of precipitates with the effects of strain energy. The colours do not represent strain distribution in a1-a3 as the contribution of strain energy is ignored. The legend thus only refers to Fig.2b1-b3.

We further studied the effects of strain energy on the necking time between two adjacent particles. Fig.3 shows the necking time for closely spaced particles versus the initial distance between them for various values of $\overline{\eta}$ for particle radii of $\overline{r} = 12$. The necking time decreased with increasing the scaled strain parameter ($\overline{\eta}$) leading to an accelerated pairing of the precipitates. When $\eta = 0$ the threshold particle spacing was identified between $\overline{d} = 18$ and $\overline{d} = 19$. Fig.4 shows a similar graph to that of Fig.3 but for particles with a radii of $\overline{r} = 21$. as is evident from Fig.4, the effects of strain

parameter was more pronounced in the case of larger particles, i.e. for $\overline{\eta} = 0.03$ with $\overline{d} = 9$ for particles with a radii of 12 the necking time occurred after $\overline{t} = 8.9 \times 10^4$, while for the similar conditions but for particles with a radii of 21 the necking time only took place after $\overline{t} = 3.2 \times 10^4$. This is because of an increase in the curvature in the case of larger particles and thus a larger tension between the two precipitates which in turn increased the strain energy and resulted in an accelerated necking.

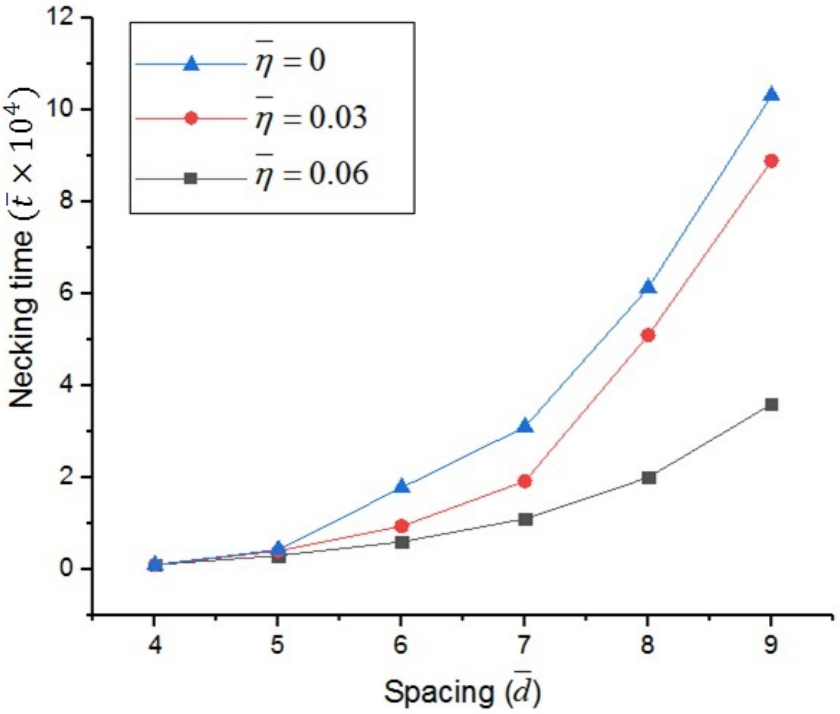

Figure 3: The necking time as a function of initial distance between two neighbouring precipitates ($\overline{r} = 12$) for different values of the strain parameter. $\overline{t}$ is dimensionless.

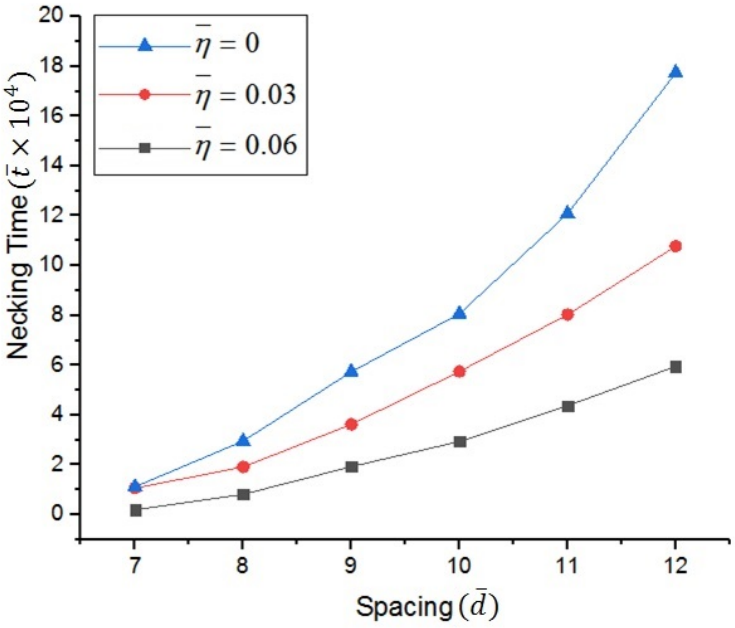

Figure 4: The necking time as a function of initial distance between two neighbouring precipitates ($\overline{r} = 21$) for different values of the strain parameter.

We performed three controlled simulations for homogeneous elasticity $h = 1$, inhomogeneous elasticity with soft particles $h = 0.5$, and hard inhomogeneous elasticity with hard particles $h = 1.5$ to examine the effect of the relative hardness/softness of particles on the pairing time. In all three cases, $\overline{\eta}$ assumed to be 0.03 and particles radii considered to be 12. The results are shown in Fig.5. Fig.5 exhibits that the necking between two adjacent particles was much more prolonged when the particles were hard compared to when they were soft, i.e. for the case where d = 12, necking time was calculated to be 17.8×10^4 when $h = 1.5$ while necking only took 5.9×10^4 to occur when $h = 0.5$. This is because the hard particles show higher resistance to deformation resulted from the tension between the particles.

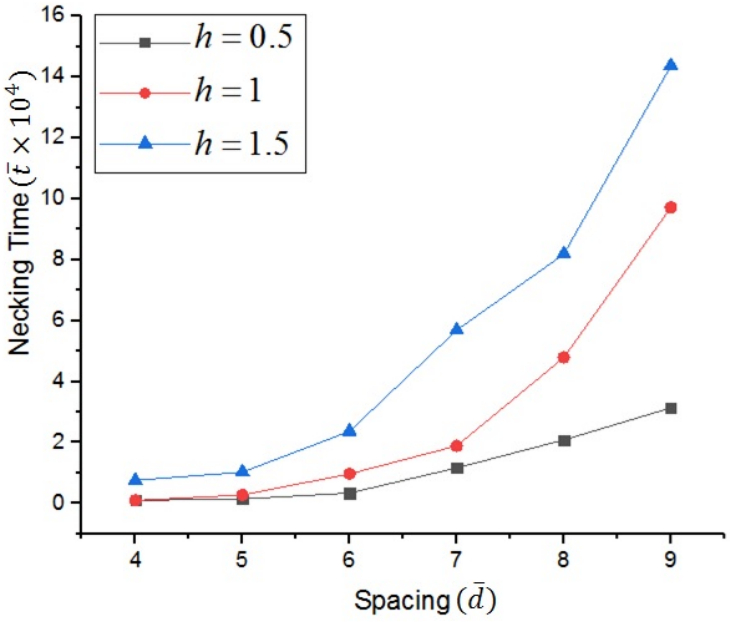

Figure 5: The necking time versus the initial spacing between two neighbouring precipitates for various values of h, with $\overline{\eta} = 0.03$ and $\overline{r} = 12$.

Fig.6a-c shows the simulation of V-composition contours during the formation of a pair in a two-particle system. The simulation results showed the formation of an intermediate phase (IP). The IP grew from the matrix and the precipitates and formed a thin IP containing crust between the precipitates. The growth of this phase affected the overall precipitating behaviour and decreased the effective spacing. Therefore, the growth of IP enhanced the necking process and thus pairing. The thickness of this phase depends on the chemical energy and the scaled strain parameter $\overline{\eta}$. After precipitates growth for certain amount of time ($\bar{t} = 8 \times 10^4$) the IP disappeared causing the formation of the paired precipitates, similar to that imaged in Fig.1 (orange box). Our simulation results in Fig.6b-c of necking precipitates show a qualitative agreement with STEM-EDS analysis in Fig.1 (black and magenta boxes). In both cases the relative EDS intensity of V in the necking region is shown to be reduced in comparison to the two initial nuclei, but significantly enriched in comparison to the bulk V concentration. The different stages of necking are imagined in the same region of the sample,

since the distance between the initial neighbouring nuclei is considerably non uniform.

Fig.6d-f shows the development of stresses within one of the neighbouring particles at a similar time step as that shown in Fig.6c for different effective spacing d. When the two particles were closely spaced ($\overline{d} = 5$) the stress distribution was at its maximum at the tip of the particle. For larger spacing $\overline{d} = 7$, the value of the stress was at a maximum at the tip, on the top and at the side of the particle. However, the stresses at the tip of a particle not only had a maximum magnitude, but, also the area bearing the maximum stresses was larger at the tip compared to that on either the top or the side of the particle. Thus, the most probable location for the pairing of the particle was again at its tip. Moreover, the development of such stresses causes the final shape of the particle to be an oblate sphere (or disk-like shape). For largely spaced particles, the location of the maximum stresses was only at the tip and the area that tolerated this stress was relatively small compared to the two other cases.

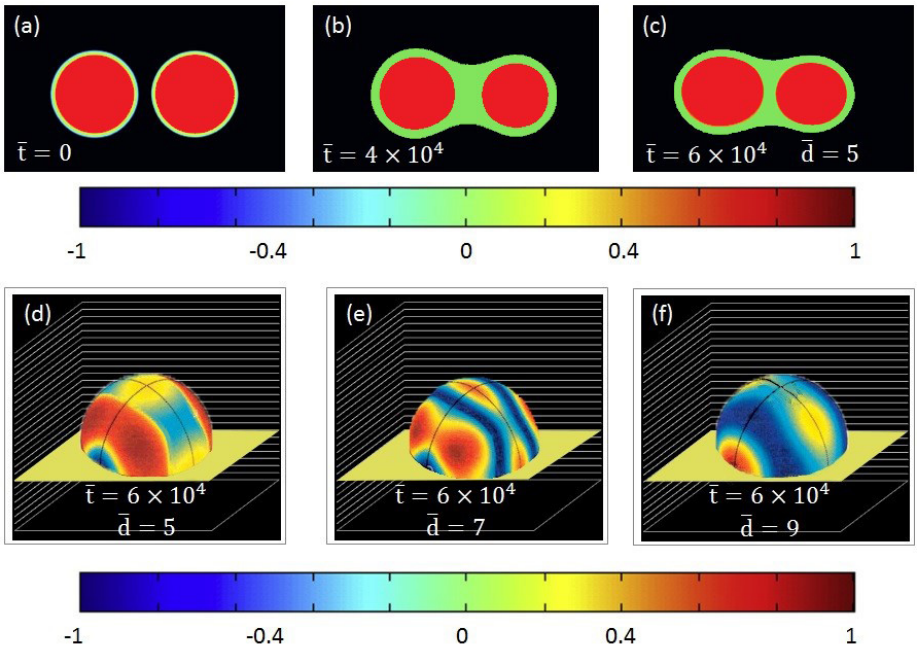

Figure 6: (a-c) Simulation results showing the distribution of V throughout the transition (The legend shows V composition contour.). The location of maximum stress of one of the neighbouring particle at the time step equal to that of shown in Fig.6c ($\bar{t} = 6 \times 10^4$) when spacing (d) $\overline{d} = 5$, (e) $\overline{d} = 7$, and (f) $\overline{d} = 9$ (The legend shows stress contours). The yellow plane marks the location of the planar interface between α and γ.

4. Conclusion

We performed phase-field simulations to study the mechanisms leading to the pairing of neighbouring precipitates in micro-alloyed steels. Our results showed that when interfacial energy was considered to be the only contributing energy, pairing of precipitates does not occur, and the dissolution of one of the particles into its neighbour was the dominating mechanism. However, when both interfacial and strain energy were included in the computation, the pairing took place because the neighbouring particles tend to minimise the strain energy. The effects of strain parameter (η) and spacing between the particles on the necking time were also studied. It was understood that the necking time decreased with increasing the strain parameter. This effect was pronounced for particles with a larger radius. We performed three controlled simulations to examine the effect of relative hardness of precipitates on the necking time. The re-

sults showed that necking is delayed significantly when the neighbouring particles are hard. The V-composition contour throughout the precipitation was simulated and the formation of an intermediate phase that facilitates necking and pairing between the two adjacent particles was observed. The location of maximum stress for different spacing was investigated and it was confirmed that the most probable location for the pairing of the particles is at their tips. This work is considered as an incremental step towards the coupled prediction of microstructural evolution and mechanical properties.

Acknowledgements

The authors are thankful to Dr Arjan Rijkenberg from Tata Steel, IJmuiden, for providing the experimental material. Financial support from the EPSRC grant EP/L018632/1 "Microstructuring micro-alloyed steels via non-metallic precipitate formation" and financial assistance from the WMG Centre High Value Manufacturing Catapult are gratefully acknowledged.

References

[1] R. W. K. Honeycombe, Transformation from austenite in alloy steels, Metall. Trans. A 7 (July) (1976) 915–936. doi:10.1007/BF02644057.

[2] T. N. Baker, Processes, microstructure and properties of vanadium microalloyed steels, Mater. Sci. Technol. 25 (2009) 1083–1107.
URL http://www.maneyonline.com/doi/abs/10.1179/174328409X453253

[3] N. Kamikawa, Y. Abe, G. Miyamoto, Y. Funakawa, T. Furuhara, Tensile Behavior of Ti,Mo-added Low Carbon Steels with Interphase Precipitation, ISIJ Int. 54 (1) (2014) 212–221. doi:10.2355/isijinternational.54.212.
URL http://jlc.jst.go.jp/DN/JST.JSTAGE/isijinternational/54.212?lang=en{&}from=CrossRef{&}type=abstract

[4] R. A. Rijkenberg, A. Blowey, P. Bellina, C. Wooffindin, Advanced High Stretch-Flange Formability Steels for Chassis & Suspension Applications 3 . Product concept : tensile properties and microstructure (2014).

[5] C. S. Smith, Microstructure: 1952 Campbell, Edward, Demille Memorial Lecture, Trans. Am. Soc. Met. 45 (1953) 533–575.

[6] G. Kurdjumov, G. Sachs, On the mechanisms of steel hardening, Z. Phys 64 (1930) 325–343.

[7] Z. Nishiyama, X-ray investigation on the mechanism of the transformation from facecentered cubic lattice to body-centered cubic lattice, Sci. Reports Res. Institutes, Tohoku Univ. 23 (1934) 637–664.
URL http://ci.nii.ac.jp/naid/10012549836/en/

[8] G. Wasserman, Einfluß der α-γ-Umwandlung eines irreversiblen Nickelstahls auf Kristallorientierung und Zugfestigkeit, Eisenhuettenwes 16 (1933) 647.

[9] H. I. Aaronson, Observations on interphase boundary structure (1974). doi:10.1111/j.1365-2818.1974.tb04640.x.

[10] P. Clemm, J. Fisher, The influence of grain boundaries on the nucleation of secondary phases, Acta Metall. 3 (1955) 70–73.

[11] H. I. Aaronson, S. K. Liu, W. T. Reynolds Jr, G. J. Shiflet, Discussion On the influence of a solute drag-like effect upon the growth of ferrite in F e - C - X alloys, J. Mater. Sci. 20 (1985) 4232–4238.

[12] K. Campbell, R. W. K. Honeycombe, The Isothermal Decomposition of Austenite in Simple Chromium Steels, Met. Sci. 8 (1) (1974) 197–203.

[13] A. Chamisa, Development of Ultra High Strength Steels for Reduced Carbon Emissions in Automotive Vehicles, Ph.D. thesis, University of Sheffield (2014).
URL http://etheses.whiterose.ac.uk/6274/

[14] A. T. Davenport, R. W. K. Honeycombe, Precipitation of Carbides at γ -α Boundaries in Alloy Steels, Proc. R. Soc. London Ser. a-Mathematical Phys. Sci. 322 (1549) (1971) 191–205.

[15] A. Rahnama, S. Clark, V. Janik, S. Sridhar, A phase-field model for interphase precipitation in V-micro-alloyed structural steels, Comput. Mater. Sci. 137 (2017) 257–265. doi:10.1007/s11661-001-0249-9.
URL http://link.springer.com/10.1007/s11661-001-0249-9

[16] L.-Q. Chen, Phase -Field Models for Microstructure Evolution, Annu. Rev. Mater. Res. 32 (1) (2002) 113–140. doi:10.1146/annurev.matsci.32.112001.132041.
URL http://www.annualreviews.org/doi/abs/10.1146/annurev.matsci.32.112001.132041

[17] D. A. Porter, K. E. Easterling, M. Y. Sherif, Phase Transformations in Metals and Alloys, third edit Edition, CRC Press, Boca Raton, 2009.
URL http://www.crcpress.com/product/isbn/9781420062106

[18] F. R. N. Nabarro, The Strains Produced by Precipitation in Alloys, Proc. R. Soc. A Math. Phys. Eng. Sci. 175 (963) (1940) 519–538. doi:10.1098/rspa.1940.0072.
URL http://rspa.royalsocietypublishing.org/cgi/doi/10.1098/rspa.1940.0072

[19] I. Steinbach, F. Pezzolla, A generalized field method for muliphase transformations using interface fields, Phys. D 134 (1999) 385–393.

[20] A. Reuss, Berechnung der Fließgrenze von Mischkristallen auf Grund der Plastizitätsbedingung für Einkristalle ., ZAMM - Zeitschrift für Angew. Math. und Mech. 9 (1) (1929) 49–58. doi:10.1002/zamm.19290090104.
URL http://doi.wiley.com/10.1002/zamm.19290090104

[21] R. Hill, Elastic properties of reinforced solids: Some theoretical principles, J. Mech. Phys. Solids 11 (5) (1963) 357–372. doi:10.1016/0022-5096(63)90036-X.
URL http://linkinghub.elsevier.com/retrieve/pii/002250966390036X

[22] J. Tiaden, B. Nestler, H. Diepers, I. Steinbach, The multiphase-field model with an integrated concept for modelling solute diffusion, Phys. D Nonlinear Phenom. 115 (1-2) (1998) 73–86. doi:10.1016/S0167-2789(97)00226-1.
URL http://linkinghub.elsevier.com/retrieve/pii/S0167278997002261

[23] J. Tiaden, U. Grafe, I. Steinbach, The prospectives of phase field modelling for the investigation of phase transformations in steel, in: Cut. Edge Comput. Simul. Solidif. Cast., 1999, pp. 13–20.

[24] S. G. Kim, W. T. Kim, T. Suzuki, Phase-field model for binary alloys., Phys. Rev. E. Stat. Phys. Plasmas. Fluids. Relat. Interdiscip. Topics 60 (6 Pt B) (1999) 7186–7197. doi:10.1103/PhysRevE.60.7186.

[25] Y. Oba, S. Koppoju, M. Ohnuma, T. Murakami, H. Hatano, K. Sasakawa, A. Kitahara, J. Suzuki, Quantitative Analysis of Precipitate in Vanadium-microalloyed Medium Carbon Steels Using Small-angle X-ray and Neutron Scattering Methods, ISIJ Int. 51 (11) (2011) 1852–1858. doi:10.2355/isijinternational.51.1852.

[26] T. Murakami, H. Hatano, G. Miyamoto, T. Furuhara, Effects of Ferrite Growth Rate on Interphase Boundary Precipitation in V Microalloyed Steels, ISIJ Int. 52 (4) (2012) 616–625. doi:10.2355/isijinternational.52.616.
URL http://joi.jlc.jst.go.jp/JST.JSTAGE/isijinternational/52.616?from=CrossRef

[27] F. Larche, J. W. Cahn, a Linear Theory of Thermochemical of Solids Under Stress, Acta Metall. 21 (1973) 1051. doi:10.1016/0001-6160(73)90021-7.

[28] A. R. Denton, N. W. Ashcroft, Vegard's law, Phys. Rev. A 43 (6) (1991) 3161–3164. doi:10.1103/PhysRevA.43.3161.

[29] M. Segawa, A. Yamanaka, S. Nomoto, Multi-phase-field simulation of cyclic phase transformation in Fe-C-Mn and Fe-C-Mn-Si alloys, Comput. Mater. Sci. 136 (2017) 67–75. doi:10.1016/j.commatsci.2017.04.014.
URL http://linkinghub.elsevier.com/retrieve/pii/S0927025617301982

[30] J. M. Howe, Interfaces in materials: atomic structure, thermodynamics and kinetics of solid-vapor, solid-liquid and solid-solid interfaces, Wiley-Interscience publication, John Wiley & Sons, New York, 1997.
URL https://books.google.co.uk/books?id=zKnvAAAAMAAJ